Structural modulations and magnetic properties of off-stoichiometric Ni-Mn-Ga magnetic shape memory alloys

A. Pramanick,[1] X. P. Wang,[1] K. An,[1] A. D. Stoica,[1] J. Yi,[2] Z. Gai,[2] C. Hoffmann,[1] and X.-L. Wang[1,*]

[1]*Chemical and Engineering Materials Division, Oak Ridge National Laboratory, Oak Ridge, Tennessee 37831, USA*
[2]*Center for Nanophase Materials Sciences, Oak Ridge National Laboratory, Oak Ridge, Tennessee 37831, USA*

A comparative description of the crystallographic structural details and the magnetic properties of Ni-Mn-Ga magnetic shape memory alloys are necessary to understand the physical origins of their magnetoelastic properties. The crystallographic structural details of an off-stoichiometric $Ni_2Mn_{1.14}Ga_{0.86}$ alloy have been obtained from the refinement of high-resolution single-crystal neutron diffraction data, following a $(3 + 1)$-dimensional $[(3 + 1)$-D] superspace formalism. In particular, the structure adopts a $P2/m(\alpha 0\gamma)00$ superspace group symmetry with the following fundamental lattice parameters: $a = 4.255(4)$ Å, $b = 5.613(4)$ Å, $c = 4.216(3)$ Å, a commensurate periodicity of 5M, and a modulation wave vector of $\vec{q} = 2/5\vec{c}$. The magnetic properties of the crystal are characterized from magnetic susceptibility measurements, as well as from neutron diffraction intensities. The overall magnetic moment per unit cell is 2.7 μ_B per $Ni_2Mn_{1.14}Ga_{0.86}$ formula unit and the magnetic moments are aligned along the b axis. The modulations of the atomic site displacements, site occupancies, and magnetic moments are elucidated from a $(3 + 1)$-D refinement of the neutron diffraction intensities. In addition to atomic displacements corresponding to shear waves along $\langle 110 \rangle$, distortions of the Ni-centric tetrahedra are also evident. Physical interpretations for the different structural distortions and their relationship to magnetic properties are discussed.

I. INTRODUCTION

Ni-Mn-Ga alloys have generated considerable interest in recent years as a new class of smart materials owing to their large magnetic-field-induced strains (up to 10%) and stress-induced changes in magnetization (up to 30%).[1–4] Ni-Mn-Ga alloys, for compositions close to the stoichiometric Ni_2MnGa compound, are ferromagnetic with a $T_C \sim 370$ K and are known to undergo multiple thermoelastic phase transformations below T_C depending on alloy compositions and thermoelastic history.[5–7] Below the martensitic phase transition temperature T_M, the alloy exhibits large structural and electronic instabilities which are also known to be coupled.[8,9] These physical traits lead to a high degree of correlation between the crystal and magnetic structures of the material and consequently to their significant magnetoelastic properties. For a fundamental understanding of the magnetoelastic properties of these alloys, it is therefore extremely important to have a comprehensive understanding of the interplay between their crystal and magnetic structures.

One of the first crystallographic analyses of a stoichiometric Ni_2MnGa compound was provided by Webster *et al.*, using neutron and x-ray diffraction on single-crystal and polycrystalline samples. The high-temperature austenite phase was described as the Heusler $L2_1$ structure belonging to the $Fm\bar{3}m$ space group, which consists of four interpenetrating face-centered-cubic (fcc) sublattices with Ni atoms occupying the $(0,0,0)$ and $(1/2,1/2,1/2)$ sites, Mn atoms occupying the $(1/4,1/4,1/4)$, sites and Ga atoms occupying the $(3/4,3/4,3/4)$ sites, the lattice parameter of the unit cell being $a_{austenite} = 5.825$ Å.[10] The structure can also be viewed as a network of Ni-centric tetrahedra with either Mn or Ga occupying the apex positions, as illustrated in Fig. 1(a). Ni-Mn-Ga is part a broader category of β alloys which undergo thermoelastic martensitic phase transformations from open body-centered-cubic (bcc) ordered structures to close-packed structures by the so-called Bain distortion.[11,12] Specifically, in Ni-Mn-Ga, the martensitic transformation is conventionally described as an inverse Bain-type distortion from an ordered $L2_1$ structure to a body-centered-tetragonal (bct), orthorhombic, or monoclinic crystal structure, depending on the specific alloy composition. Originally it was reported that in stoichiometric Ni_2MnGa, on cooling below 202 K, the structure undergoes a tetragonal modification of the parent $L2_1$ phase, the lattice parameters of the tetragonal unit cell being given by $c_{martensite} = 5.566$ Å and $a_{martensite} = 5.920$ Å, with $c/a = 0.940$.[10] In addition to the principal diffraction peaks resulting from the bct structure, weak diffraction spots— superlattice peaks or satellites—could also be observed. The presence of these additional diffraction spots was interpreted as an evidence for periodic stacking faults which lead to a superstructure with a certain periodicity along the c axis.[10,13]

Long-period stacking of close-packed planes has been reported for many crystal structures of β-phase intermetallic martensites such as NiAl and NiAlMn.[14–17] The structure of these martensitic alloys could be viewed as a stacking of $\{110\}$-austenite planes in a zigzaglike arrangement, with each subsequent layer being displaced from its preceding layer by a certain distance along the $[1\bar{1}0]$ direction and with exact matching of the atomic positions for every nth layer ($n = 5, 7, 10, 12,$ or 14). The relative displacements between the subsequent planes can be obtained through refinement by matching the calculated intensities from the proposed structure factor with the measured intensities of the superlattice peaks. For example, the structure for $Ni_{50}Al_xMn_{50−x}$ ($x \geqslant 19$) martensite has been described as 10M, in which the stacking sequence is repeated over 10 units of the average basic bct cell.[14,15] In Zhdanov notation, this particular stacking sequence is described as $(3\bar{2})_2$, whereby three subsequent atomic layers
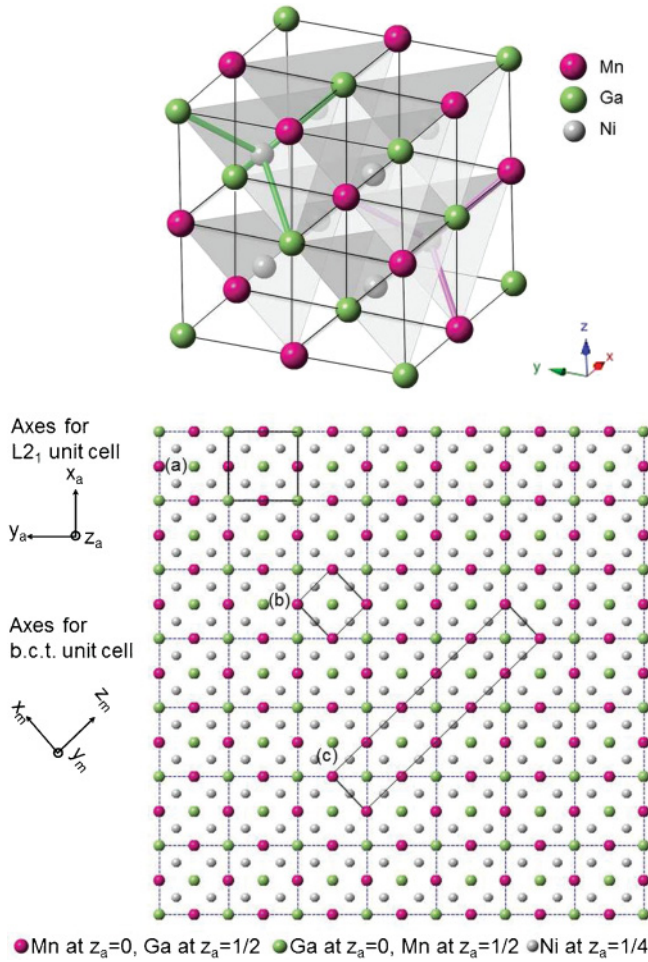
FIG. 1. (Color online) (a) View of the austenite $L2_1$ unit cell of cubic Ni$_2$MnGa. The Ni atoms sit at the centers of the Ni-Mn and Ni-Ga tetrahedra. The Ni-Mn bonds within a tetrahedron are shown in pink, while those of Ni-Ga are shown in green. (b) The orientation relationship between (a) the $L2_1$ structure, (b) the bct martensitic structure, and the modulated superstructures of (c) 5M. The modulation of the atomic positions and properties in the superstructure extend mainly along the z_m direction.

are displaced along a certain direction and the next two subsequent atomic planes are displaced in the opposite sense, and the pattern is repeated twice to complete one unit cell of the superstructure.[11] The stacked nature of the martensite structure is sometimes interpreted as an adaptive phase made of nanoscale twins.[18,19]

Following a different interpretation, the atomic positions within these martensitic superstructures were described as a periodic modulation of the atomic planes along [1$\bar{1}$0] axes on (110) planes of the cubic structure of the original austenite. The displacement Δ_j of the jth plane from its regular position along the modulation direction can be given as a Fourier series,

$$\Delta_j = \sum_{n=1}^{3} A_n \sin (2\pi j/L), \qquad (1)$$

where L is the number of layers within a single modulation period.[13] Such shuffling of lattice planes can be viewed as a static wave of shear displacements following the (110)

[1$\bar{1}$0] scheme for displacement. In a more refined description of the crystal structure, individual atomic sites (rather than lattice planes) could be allowed to modulate with the same periodicity but with different displacement amplitudes.[16] The static modulation of atomic positions in the martensite phase could be interpreted as a condensation of the soft phonons of the TA$_2$ acoustic phonon branch with wave vector $\vec{q} \| \langle 110 \rangle$ and polarization vector $\vec{e} \| \langle 1\bar{1}0 \rangle$. This was evidenced from the gradual change of the modulation period as the cubic $L2_1$ structure morphs into premartensite phases before a final transition to a layered martensitic structure.[20]

Subsequent structural investigations revealed that the symmetry of the martensitic phase of Ni-Mn-Ga could be better described as a superstructure of a bct unit cell, which has the following relations to the axes of the parent $L2_1$ austenite phase: $c_m \| [1\bar{1}0]_a, a_m \| [110]_a, b_m \| [001]_a$, where the subscripts m and a refer to the martensite and the austenite phases, respectively. In the superstructure, structural modulations extend principally along the c_m axis. Different modulated structures, such as 5M, 7M, and 10M, have been reported for Ni-Mn-Ga, depending on the number of bct unit cells within one period of the superstructure.[5,21–27] The relationship between the austenite $L2_1$ phase, the bct unit cell and the 5M superstructure is shown in Fig. 1(b).

Since Ni-Mn-Ga alloys exhibit a large degree of coupling between their structural and electronic orders, it can be expected that their magnetic structures also exhibit a certain modulation in relation to the modulation of structural displacements. Moreover, the occupancies for the different sites in off-stoichiometric compositions are expected to have some correlations with structural and magnetic modulations. It can be noted that the best magnetoelastic properties of Ni-Mn-Ga are obtained for off-stoichiometric compositions,[2,28,29] and therefore a detailed determination of the structural and magnetic configurations in off-stoichiometric alloys is of particular significance for materials with potential applications.

The use of $(3+1)$-dimensional [$(3+1)$-D] superspace formalism was earlier demonstrated as a powerful method for determination of structural, compositional, and physical modulations in many commensurate and incommensurate superstructures.[30–33] In this formalism, the modulation is described in terms of a parameter, p, in $(3+1)$-D space,

$$p(\bar{x}_4) = p(t + k_1\bar{x}_1 + k_2\bar{x}_2 + k_3\bar{x}_3), \qquad (2)$$

where $\bar{x}_i$ are the different dimensions, t is the "phase" of the modulation, and $\bar{x}_4$ is a function of t and $\bar{x}_i$. The modulated lattice in the 3D space R_3 can be viewed as a section through the structure in the $(3+1)$-D space R_4, when the parameter t,

$$t = -k_1\bar{x}_1 - k_2\bar{x}_2 - k_3\bar{x}_3 + \bar{x}_4, \quad \text{or}$$
$$t = -\vec{q} \cdot \vec{r} + \bar{x}_4, \qquad (3)$$

is equal to zero. For a more detailed description, please refer to the Appendix. This method is effective in the sense that it allows modulations of multiple properties of a superstructure with correlated refinement parameters to arrive at a convergent solution. In the case of Ni-Mn-Ga, the $(3+1)$-D superspace formalism was applied to obtain structural modulations in alloys of different compositions.[24,26,27] In our work, we have implemented this approach to determine not only the structural

but also compositional and magnetic modulations within a 5M commensurate superstructure of $Ni_2Mn_{1.16}Ga_{0.84}$, thereby providing a broader physical insight into the interrelations between structure and magnetism in this material.

II. EXPERIMENTAL PROCEDURE

Single-crystal samples of Ni-Mn-Ga alloys were obtained from AdaptaMat Ltd. with dimensions of $8 \times 8 \times 15$ mm. The composition of the samples was 50 at.%Ni, 28.5 at.%Mn, 21.5 at.%Ga (± 0.5 at.%). Martensite transformation temperatures are $T_M = (M_s + M_f)/2 = 48\,°C$, $T_A = (A_s + A_f)/2 = 54\,°C$, $M_s - M_f \approx A_f - A_s \approx 3$ K. The Curie temperature is $T_C = 99\,°C$. Magnetic field ~ 1 T was applied at ambient temperature for training of the twin microstructure so as to obtain a single twin variant.

Magnetic properties of the material were characterized with a Superconducting Quantum Interference Device (SQUID)-based Quantum Design magnetic property measurement system (MPMS). The temperature dependences of the magnetization were measured at fields of 1 and 100 Oe during heating and cooling cycles in the temperature range of 5 K to 400 K, respectively. The field dependences of the magnetization were measured at 300 K within an extended dynamic range.

A. Diffraction measurements

Initial characterization of the crystal was made on the VULCAN instrument at the Spallation Neutron Source (SNS) of the Oak Ridge National Laboratory using the original size of the single crystal.[34–36] Diffraction measurements were taken parallel to the [001], [100], and [010] crystallographic axes of the $L2_1$ cell, as shown in Fig. 2, from which the basic unit cell parameters were obtained. Splitting of the $\{200\}_m$ diffraction peaks indicate a multidomain structure of a noncubic phase. Furthermore, from the relative splitting of the $\{101\}_m$ peaks, the angle between the [001] and the [100] axes was determined to be $\sim 90.3°$. This indicates the monoclinic distortion of the $L2_1$ unit cell. In addition to these principal peaks, satellites were observed between the various orders of the hkl peaks, which indicated the presence of a superstructure. However, precise determination of the structural/magnetic superstructure required comprehensive survey of the reciprocal space. This was done at the SNS TOPAZ single-crystal diffractometer at room temperature in the wavelength-resolved time-of-flight (TOF) Laue mode, using neutron wavelengths in the range of 0.65 to 3.4 Å.[37] Unlike a conventional Laue diffractometer on a reactor source, where neutrons coming from closely aligned twins are recorded indiscriminately, time-of-flight diffractometers on a pulse neutron source can resolve the diffraction peaks from different twin variants in both space and time.[38] Thus, even for domains with their crystallographic axes closely aligned, on a time-of-flight diffractometer such as TOPAZ, their diffraction intensities appear at different times of flight that correspond to different neutron wavelengths, thereby resulting in discrete, separate reciprocal lattices. These can be analyzed individually. For this measurement, a smaller single crystal of dimensions $2.5 \times 2.5 \times 2.1$ mm was cut from the original crystal using electrical-discharge machining. The TOPAZ instrument uses an array of neutron wavelength-
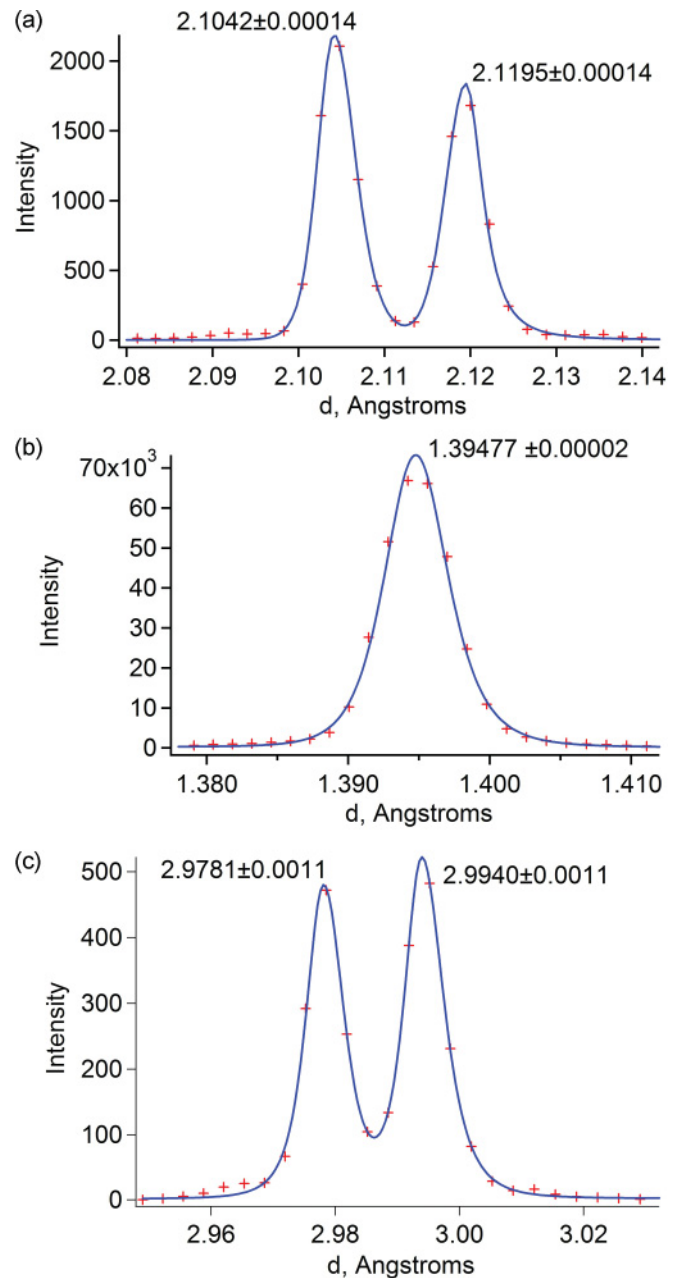

FIG. 2. (Color online) (a) $\{200\}_m$, (b) $(040)_m$, and (c) $\{101\}_m$ diffraction peaks collected on VULCAN. The lattice parameters from single peak fitting are shown.

resolved 2D area detectors at distances 39.5 to 45.0 cm from the sample. Each detector module has an active $150 \times 150\,mm^2$ area that is divided into 256×256 pixels (0.578 mm/pixel). Raw data were recorded in the neutron event mode with time intervals of 1 μs, which is equivalent to a neutron wavelength resolution of 2.15×10^{-4} at 1.0 Å. Currently TOPAZ has 14 area detectors installed on the surface of a spherical detector array with angular coverage $\pm 32°$ from the horizontal plane and detector 2θ angles from $18.0°$ to $144.0°$. During data collection, the neutron event data were saved and broadcasted to a listening server in a local EVENTVIEWER program in ISAW[39] for live viewing of the measured diffraction data in a 3D q space. The EVENTVIEWER program can be used for
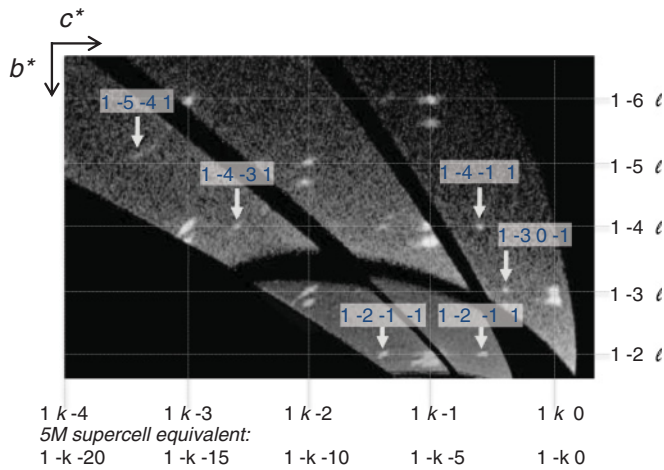
FIG. 3. (Color online) Section of the reciprocal lattice showing selected diffraction spots of the crystal collected on multiple detector modules of TOPAZ for one particular orientation of the crystal. The reciprocal lattice is indexed following the 5M supercell parameters. The superlattice peaks along $\mathbf{c}^*$ are indicated by arrows. $\mathbf{a}^*$ projects into the paper.

indexing peaks, generating an orientation matrix and carrying out data integration in real time. The orientation matrix from initial indexing of the single-crystal sample was imported into the CRYSTALPLAN program[40] for data collection strategy optimization. Diffraction data for the crystal were collected in 7 h using ten different sample orientations with different angular settings. The Bragg peaks from each angular setting were integrated in the event mode in a 3D q space using a 5M supercell of the basic unit cell that was obtained from VULCAN measurements and the corresponding TOPAZ orientation matrix; a 5M supercell could be justified from earlier reports on similar composition,[26] and current measured diffraction patterns. All recorded Bragg reflections could be initially indexed following this scheme for a 5M supercell. A section of the reciprocal lattice, collected on multiple TOPAZ detector modules for a single orientation of the crystal, is shown in Fig. 3. The superstructure peaks along $\mathbf{c}^*$ are marked by arrows. While the measured diffraction patterns showed the presence of multiple twins, reflections from one twin variant were identified according to the orientation matrix, integrated, and subsequently used for structure refinement.

The measured diffraction patterns for Ni$_2$Mn$_{1.14}$Ga$_{0.86}$ showed no indication for body centering. The space group $P2/m$ with $a = 4.255(4)$ Å, $b = 5.613(4)$ Å, and $c = 21.082(13)$ Å, $\beta = 90.42(5)°$ was chosen, which is different from the $I2/m$ space group reported for the parent compound Ni$_2$MnGa.[24] Data reduction was performed using the local ANVRED2 program in ISAW. The nuclear structure for Ni$_2$Mn$_{1.14}$Ga$_{0.86}$ was obtained from those reported for Ni$_2$MnGa by expanding the unique atoms of the $I2/m$ space group to $P2/m$ and using them as the starting positions for structural refinement in JANA2006.[41] Subsequent refinement of the positional and occupancy factors for Ni$_2$Mn$_{1.14}$Ga$_{0.86}$ in the $(3 + 1)$-D superspace setting using high-angle reflections yielded a result that was consistent with a

TABLE I. Experimental details and refined crystallographic data for Ni$_2$Mn$_{1.14}$Ga$_{0.86}$.

Sample	Ni$_2$Mn$_{1.14}$Ga$_{0.86}$
Measurement parameters	
Radiation type	Neutron
Source	Spallation neutron source
Measurement device	TOPAZ
Measurement device type	Wavelength-resolved Laue
Diffraction detector	Neutron anger cameras
Wavelength range	0.65–3.4 Å
θ_{min}	4.08°
θ_{max}	56.72°
Temperature	25 °C
Refinement parameters	
Total number of reflections	854
No. of reflections ($I > 3\sigma(I)$)	543
Total No. of parameters	64
No. of constrained parameters	24
Crystal structure	
Space group	$P2/m$, No. 10, unique axis: b
Modulation period	2/10
a (Å)	4.255(4)
b (Å)	5.613(4)
c (Å)	4.216(3)
β (°)	90.41(5)
Volume (Å^3)	100.70(14)
Z	2
Calculated density (g cm^{-3})	7.9116
Calculated formula	Ni$_2$Mn$_{1.14}$Ga$_{0.86}$
Agreement factors	
R factor[a] ($I > 3\sigma$, all)	0.0934, 0.1598
wR factor[b] ($I > 3\sigma$, all)	0.0768, 0.0976
Goodness of fit	1.86

[a] $R = \sum ||F_O| - |F_C||/ \sum |F_O|$.
[b] $wR = \sum w||F_O| - |F_C||/ \sum w|F_O|$, where $w = 1/(\sigma(F_O)^2 + 0.0001 F_O^2)$. Goodness of fit $S = \sqrt{\frac{w(F_O - F_C)^2}{m-n}}$, where m is the number if reflections and n is the number of parameters refined, F_O is the observed structure factor and F_C is the calculated structure factor.

commensurate structure in the space group $P2/m$ with $\vec{\mathbf{q}} = {}^2/_5\vec{\mathbf{c}}$. The positions of selected superlattice peaks are shown in Fig. 3, which are indexed according to the $(3 + 1)$-D superspace formalism. The equivalent 5M supercell equivalent indices along $\mathbf{c}^*$ are also shown for comparison. Low-angle reflections were then included for magnetic structural analysis. The moments [ferromagnetic with $\mathbf{k} = (0,1,0)$] for Mn atoms at $(0,0,0)$ and $(1/2,1/2,1/2)$ positions and their modulation waves were refined in the magnetic space group $P2/m(\alpha 0\gamma)00$ using the $(3 + 1)$-D superspace approach in JANA2006. The final refinement converged to $R1 = 0.0976$ and $wR1 = 0.0768$ for 543 reflections with $I_o > 3\sigma(I)$. Crystal data for Ni$_2$Mn$_{1.14}$Ga$_{0.86}$ are listed in Table I. The atomic positions and amplitudes of the modulation function of the commensurate modulated phase are listed in Table II.

TABLE II. Atomic positions and amplitudes of the modulation function for the different sites of the 5M commensurate phase.

Name	Atom	Wyck.		x	y	z	Site occ.	U_{iso} equiv.
Mn1	Mn	a		0	0	0	1	0.0212(12)
			A_1	0.0709(17)		0.0034(8)		
			A_2	0.0074(15)		–0.0074(10)		
Ga1	Ga	b		0	0.5	0	0.854(9)	0.0196(9)
			A_1	0.0546(10)		0.0007(6)	–0.034(5)[a]	
			A_2	0.0100(9)		0.0107(7)	–0.007(6)[a]	
MnGa1[b]	Mn	b		0	0.5	0	0.146(9)	0.0196(9)
			A_1	0.0546(10)		0.0007(6)	0.034(5)[a]	
			A_2	0.0100(9)		0.0107(7)	0.007(6)[a]	
Ga2	Ga	g		0.5	0	0.5	0.866(9)	0.0397(15)
			A_1	0.0612(18)		0.0009(11)	–0.051(7)	
			A_2	–0.0037(14)		–0.0109(11)	0.042(9)	
MnGa2	Ga	g		0.5	0	0.5	0.144(9)	0.0397(15)
			A_1	0.0612(18)		0.0009(11)	0.051(7)	
			A_2	–0.0037(14)		–0.0109(11)	–0.042(9)	
Mn2	Mn	h		0.5	0.5	0.5	1	0.0281(16)
			A_1	0.0497(19)		–0.0029(12)		
			A_2	0.0150(18)		0.0185(14)		
Ni1	Ni	$2j$		0.5	0.2481(2)	0	1	0.0239(4)
			A_1	0.0674(6)	–0.0063(2)[a]	–0.0009(3)		
			A_2	0.0137(5)	–0.0091(3)[a]	0.0018(3)		
Ni2	Ni	$2k$		0	0.2500(2)	0.5	1	0.0255(5)
			A_1	0.0509(6)	–0.0069(2)[a]	0.0051(3)		
			A_2	–0.0069(5)	–0.0030(2)[a]	–0.0059(4)		

[a]These values are for the coefficient of the cosine terms. The values in the row for A_1 and A_2 correspond to the coefficients B_1 and B_2, respectively. For nonzero values of B (A), the corresponding values for A (B) are equal to zero.
[b]MnGa1 means Mn substituted on Ga1 sites. Similarly for MnGa2.

III. RESULTS

A. Magnetic characterization

Magnetization of the single-crystal sample was measured as functions of temperature and magnetic field, with the external field applied along the [010] direction of the sample. Figure 4(a) depicts the remnant magnetization ($H = 1$ Oe) as a function of temperature during cooling from 400 K to 5 K. For measurement with the magnetic field applied along the [010] direction, the sample starts to show ferromagnetic ordering at $T_C = 372$ K. A sharp decrease in remnant magnetization is observed at the martensitic phase transition temperature of $T_M = 320$ K. A broad decline in the magnetization is also observed around 200 K, which is indicative of a second-order intermartensitic phase transition. Intermartensitic phase transition in off-stoichiometric Ni-Mn-Ga alloy has also been reported earlier.[42] Figure 4(b) shows temperature dependence of the remanent magnetization during cooling and heating for an applied field of $H = 100$ Oe. The martensitic transition temperature T_M on the cooling curve and austenitic transition temperature T_A on the heating curve are determined to be 320 K and 334 K, respectively.[43]

Both the martensitic and the austenitic phases coexist in between 320 K and 334 K. The existence of a thermal hysteresis during warming and cooling around T_c is a signature of the first-order nature of the ferromagnetic transition.[44] The field-dependent magnetization curves of the sample at 300 K are shown in Fig. 4(c), where the material is in the ferromagnetic martensite phase. The magnetization of the sample is fully saturated at an applied field of 1.0 T along [010]; the saturation magnetic moment at 300 K is 2.67 μB per formula unit of $Ni_2Mn_{1.14}Ga_{0.86}$. Consistent with previous reports, the isothermal sweep curves are essentially reversible as the magnetic hysteresis is found to be very small [red and blue curves in Fig. 4(c)]. The relatively low field of 1 T for ferromagnetic saturation is attractive from the viewpoint of practical applications.

B. Crystal and magnetic structure refinement

Basic symmetry and structure parameters. The refinement results and the basic crystallographic data for $Ni_2Mn_{1.14}Ga_{0.86}$ are listed in Table I. The final convergence is achieved with the unit cell constants of $a_m = 4.255(4)$ Å, $b_m = 5.613(4)$ Å, and
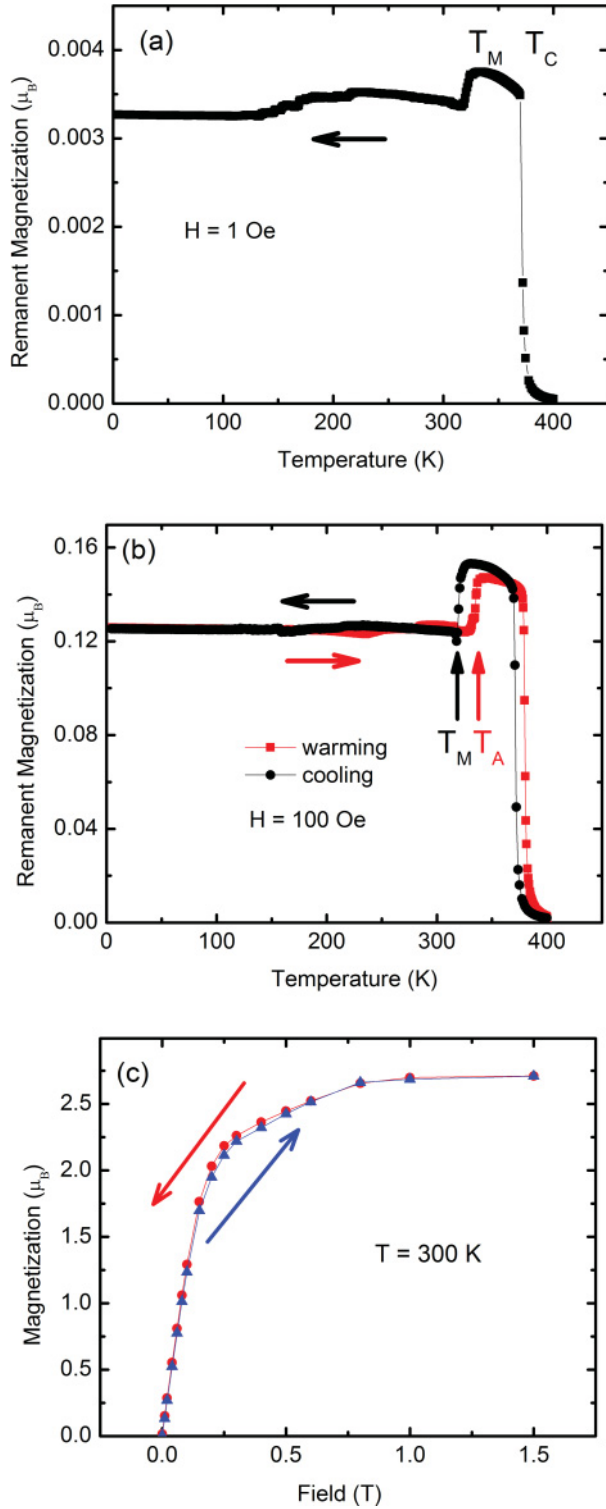
FIG. 4. (Color online) Magnetizations of the single-crystal sample as functions of temperature and magnetic field with external field applied along the [010] direction of the sample. (a) Temperature-dependent remanent magnetization of the sample at $H = 1$ Oe measured during cooling down from 400 K to 5 K. (b) Cooling down (black) and warming up (red) magnetizations at $H = 100$ Oe. (c) Magnetization (blue) and demagnetization curves (red) at 300 K.

$c_m = 4.216(3)$ Å, $\beta = 90.41(5)°$. These values are very close to those reported by Righi *et al.* for superspace refinement of

x-ray powder patterns for $Ni_2Mn_{1.15}Ga_{0.85}$,[26] except for the absence of body centering in the current refined structure. However, the $P2/m$ symmetry is consistent with previous neutron diffraction refinements of single crystal patterns of $Ni_{50.5}Mn_{28.2}Ga_{21.3}$.[21] The high-resolution neutron diffraction pattern from a single crystal used in this study confirms the $P2/m$ symmetry. A small monoclinic distortion is further confirmed by splitting of the $\{101\}_m$ diffraction peaks; fitting of high-resolution $\{101\}_m$ peaks collected on the VULCAN diffractometer (as shown in Fig. 2) gives a value of $\sim 90.3°$, which is close to the value of $90.41(5)°$ obtained from the refinement of the single-crystal TOPAZ data.

Modulation of atomic positions and site occupancies. The displacement modulation function of the atoms $\vec{u}(\bar{x}_4)$ from their generic average position $\bar{x}_i$ in the basic structure is modeled following

$$x_i = \bar{x}_i + \vec{u}(\bar{x}_4),$$

$$\vec{u}(\bar{x}_4) = \sum_{n=1}^{2} A_n \sin(2\pi n \bar{x}_4) + \sum_{n=1}^{2} B_n \cos(2\pi n \bar{x}_4),$$

(4)

where $\bar{x}_i$ indicates the atomic position in the basic structure and A_n and B_n are the amplitudes of the displacement modulation. Equation (4) is a classical way to describe various modulated structures including martensites.[13,16,24] $n = 2$ is justified by the presence of second-order satellites in the diffraction pattern. In the current refinement, modulations of the atomic positions were permitted along all the three dimensions, viz., x, y, and z. In addition, the site occupancies were refined to determine where the additional Mn atoms for the off-stoichiometric composition are incorporated. The additional Mn atoms were found to substitute only on the Ga sites. This was the same result proposed by Righi *et al.*;[26] however, that observation could not be confirmed until now since Mn and Ni have similar x-ray scattering factors. Here, the occupancy of the different sites could be unambiguously determined from neutron diffraction, owing to the significant differences between the bound coherent neutron scattering lengths of 10.3(1) fm, $-3.750(18)$ fm, and 7.288(2) fm for Ni, Mn, and Ga, respectively.[45]

The parameters A_n and B_n for the different atomic sites are listed in Table II. The values for B_n are insignificant, except where it is marked by an asterisk. The largest displacement amplitudes are along a, although small displacements along b and c (for Ni) can also be noted. The largest displacement amplitudes are for Mn at (0,0,0) and Ni at (0.5, 0.2481(2), 0), with $A_1 \sim 0.07$, while the maximum displacement for Ga is for site Ga2 at (0.5,0,0.5) with $A_1 \sim 0.06$. The amplitude parameters are in the same range as reported by Righi *et al.*[26] Figure 5 shows the $\bar{x}_4$ contour plots for the different sites. As explained under Sec. II, the commensurate structure in 3D can be viewed as a projection of the $(3 + 1)$-D structure along $\bar{x}_4$. The commensurate sections on the $\bar{x}_4$ contour plots for the different sites are accordingly marked at multiples of 2/5 along $\bar{x}_4$ in Fig. 5.

In addition to the atomic displacements, the substitution of Mn atoms at Ga sites is also modulated. Equation (4) is also used to model the modulation of the Ga site occupancies, as shown in Figs. 6(a) and 6(b). In the $\bar{x}_4$ plot, the occupancies
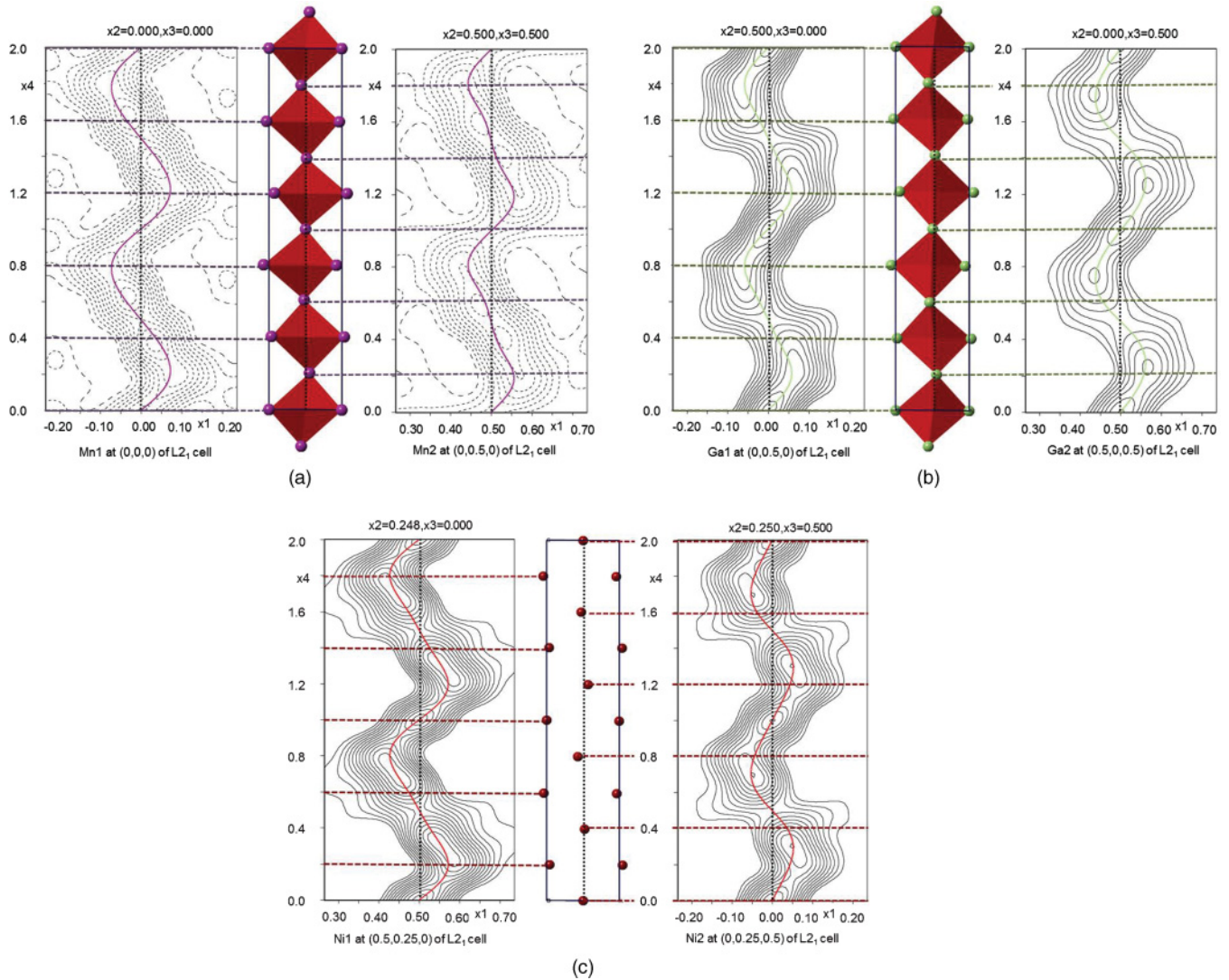
FIG. 5. (Color online) The displacement of the (a) Mn, (b) Ga, and (c) Ni atoms from their average lattice positions, shown as $\bar{x}_4$ contour plots. The dashed lines represent the sections corresponding to the commensurate lattice in R_3. For Mn and Ga, the corresponding Ni-centric tetrahedra are also shown.

of the Ga sites along the different atomic planes are indicated by the dotted lines.

Modulation of magnetic moments. Previous neutron diffraction refinements of the magnetic structure of Ni-Mn-Ga alloys indicated that most of the magnetic moment lies with the Mn atoms, while the Ni atoms are only associated with a small magnetic moment.[5,10,46] In the present refinement, it is assumed that the overall magnetic moments for the Mn atoms (at sites Mn1 and Mn2) are the same, since they are in similar environments. However, it is imperative from the modulation of the atomic positions and the occupancies that the local environments of the individual Mn atoms are different. Therefore, the magnetic moments on the individual Mn atoms were allowed to be modulated in the refinement, while constraining the overall magnetic moment on the two different sites of the average structure to be the same. The moments on the mixed Ga/Mn sites were fixed to a small value. The starting value for the overall moment per $Ni_2Mn_{1.14}Ga_{0.86}$ formula unit was set to 2.67 μ_B following the macroscopic magnetic measurements. Final convergence was achieved with

the following results for magnetic moments on individual sites:

$$\text{Mn1}: 2.779023 - 0.684254 \times \cos(2\pi\bar{x}_4),$$
$$\text{Mn2}: 2.779033 + 1.045234 \times \cos(2\pi\bar{x}_4),$$
$$\text{Ni1, Ni2}: -0.059813,$$
$$\text{MnGa1, MnGa2}: -0.049220, \qquad (5)$$

where all units are in μ_B. The modulations of the magnetic moments on the Mn sites are shown in Figs. 7(c) and 7(d). The refinement results suggest that the magnetic moment on individual Mn atoms vary from ~2 to ~3.75 μ_B. This is consistent with information from previous polarized neutron measurements and first-principle calculations.[46,47]

IV. DISCUSSION

The magnetic measurement presented in Fig. 5 shows the development of a ferromagnetic order in the present alloy below 372 K; this is consistent with previously reported
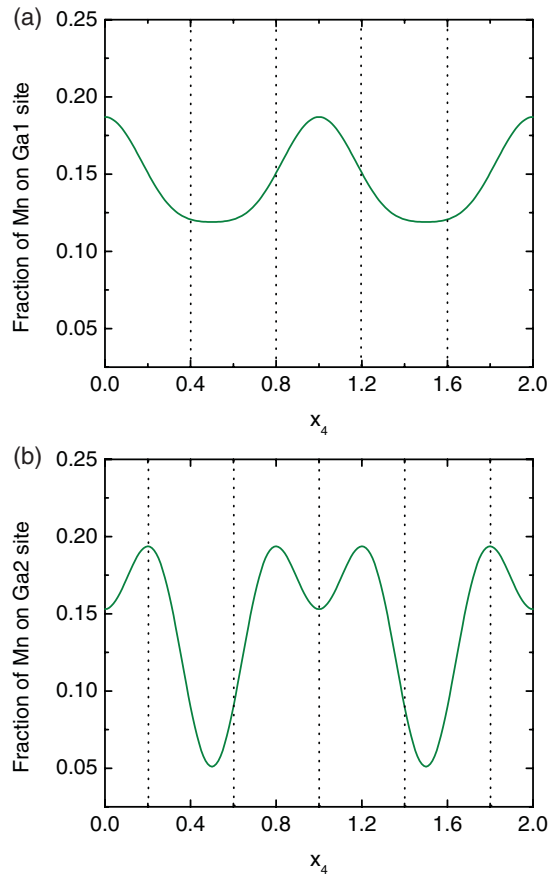
FIG. 6. (Color online) The modulation of the fraction of Mn on (a) Ga1 and (b) Ga2 sites. The dashed lines represent the sections corresponding to the commensurate lattice in R_3.

TABLE III. The average Ni-Ga and Ni-Mn bond distances for the 5M phase of $Ni_2Mn_{1.14}Ga_{0.86}$.

	Average (Å)	Maximum (Å)	Minimum (Å)
Mn1-Ni1	2.543(9)	2.496(7)	2.579(10)
Mn2-Ni1	2.549(5)	2.467(6)	2.625(6)
Ni1-Ga1	2.555(8)	2.487(8)	2.603(7)
Ni1-Ga2	2.537(4)	2.470(5)	2.585(5)

patterns shown in Fig. 5. Moreover, the modulation of the site positions along y and z are permitted in monoclinic symmetry. In the current refinement, convergence is reached with inclusion of positional modulations along the b and c directions, which yielded significant nonzero values in some cases, unlike previous x-ray diffraction investigations. It was indeed possible to determine individual atomic displacements with high accuracy, particularly for Ni and Mn, from neutron diffraction intensities (as compared to x rays) due to the large differences between their neutron scattering lengths. These differences are noteworthy from a physical point of view, as illustrated below.

Similar modulation amplitudes for all the atomic sites would imply that all the atoms located on a single {100} plane are uniformly displaced from their average lattice positions. Physically, this picture conforms to a model where layers of uniformly distorted nanometer-sized twins alternate in an adaptive phase, as described in the Introduction. However, if the amplitudes for displacive modulations are indeed different for the different atomic sites, it discards the nanotwin model and instead indicates that the modulations originate from unstable soft-mode phonons. A thorough description of the displacive modulations of the different sites, as presented in Fig. 5, illustrates the individual displacive modulations for each atomic site. This demonstrates that the nanotwin model for a 5M $Ni_2Mn_{1.14}Ga_{0.86}$ single crystal is not applicable. Previous neutron[46] and x-ray[23] diffraction studies also indicated nonconformity with the nanotwin structural model, although they did not present a thorough analysis of the displacive modulation for the different atomic sites. Apart from nonuniform atomic displacements along the a direction, an even more interesting feature is significant displacements of some of the atoms along the b and c directions. This introduces further distortions to the crystal lattice in addition to displacive modulations along a. Note that significant displacements along b exist only for the Ni atoms.

The nonuniform displacement of the different atomic sites along a and additional displacements along b and c directions can be described as a result of superpositions of two different contributions: a wavelike displacive modulation originating from soft mode phonons and distortions of tetrahedral cages around Ni.[48] For example, the distortions of the Ni-centric tetrahedra for two different subunits of the 5M supercell are shown in Fig. 8. The physical origins of tetrahedral distortions have been linked to shorter Ni-Ga bonds, as observed in extended x-ray-absorption fine structure (EXAFS)[49] and computational studies.[48,50] The *average* Ni-Ga and Ni-Mn bond distances (Table III), are in agreement with this view. However, a closer look at the structure of interpenetrating Ni-centric tetrahedra revealed that *all* the Ni-Ga bonds cannot

ferromagnetic transition temperatures of 360 K–380 K for a wide range of compositions of Ni-Mn-Ga alloys. The martensitic phase of $Ni_2Mn_{1.14}Ga_{0.86}$ is therefore in a ferromagnetic state at 300 K, where all the structural measurements were obtained.[9]

For the present alloy of composition $Ni_2Mn_{1.14}Ga_{0.86}$, the basic unit cell is primitive monoclinic with $\beta \sim 90.4°$. This is typical for Ni-Mn-Ga alloys with 5M modulated structures.[21,22,26] However, the modulation characteristics for the different atomic positions as reported here is different than that of a body-centered 5M structure of $Ni_2Mn_{1.15}Ga_{0.85}$ that was reported earlier based on superspace refinement of x-ray diffraction pattern.[26] In this earlier report, the first-order modulation amplitudes along the x direction ($\langle 1\bar{1}0 \rangle_{cubic}$) for all the atomic sites in an $I2/m$ structure are nearly equal ($A_1 \sim 0.070$), while the second-order modulation amplitudes A_2 are at least an order of magnitude lower. From the current refinement results (see Table II), one can clearly distinguish between the first-order modulation amplitudes for the different atomic sites, with A_1 ranging from ~ 0.05 to ~ 0.07. It is also noteworthy that the second-order modulation amplitudes A_2 inversely scale with respect to A_1; that is, A_2 is significantly higher when A_1 has a relatively low value. In other words, the modulations for the different sites across the same set of planes are less uniform and in some cases deviate from a single-order sinusoidal pattern. This is evident from the
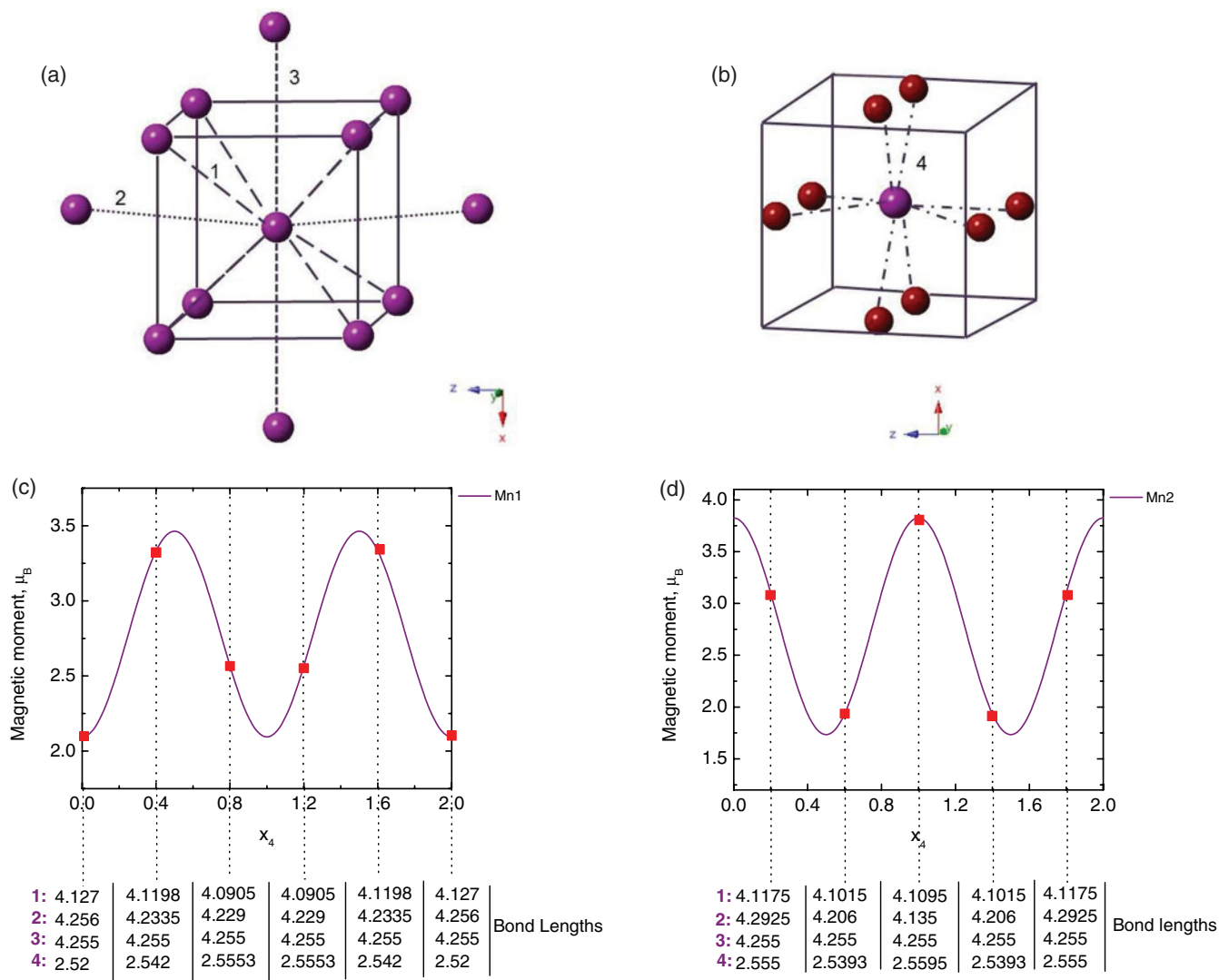
FIG. 7. (Color online) (a),(b) The different interatomic bond distances affecting the magnetic interactions with Mn atoms are indicated. The different types of Mn-Mn and Mn-Ni bonds are marked with numbers 1–4. (c),(d) The modulation of magnetic moments on Mn1 and Mn2 sites. The actual values for commensuarte sections are marked with red squares. The average distances for the interatomic bonds 1–4 are also shown for each commensuarte section.

be systematically be shorter than the Ni-Mn bonds. This is clearly evident from the example of two sets of tetrahedra shown in Fig. 8. For Ni at $\bar{x}_4 = 0$, the Ni-Mn bond distances range from 2.4964 to 2.6122 Å, while the Ni-Ga bond distances range from 2.4704 to 2.6033 Å. Similarly, for Ni at $\bar{x}_4 = 0.8$, the Ni-Mn bond distances range from 2.5393 to 2.5580 Å, while the Ni-Ga bond distances range from 2.4867 to 2.5610 Å. Hence, the previous picture for tetrahedral distortions needs to be clarified in light of the insights gained from the neutron single-crystal structure. Each tetrahedron consists of two shorter and two longer bonds. The differences in lengths between the shorter and the longer bonds are larger, on average, for Ni-Ga tetrahedra than for Ni-Mn tetrahedra. Therefore, although the system strives to achieve smaller Ni-Ga bond lengths on average, the Ni-Ga tetrahedra are more distorted compared to Ni-Mn tetrahedra.

In Ni-Mn-Ga alloys, strong correlations between the lattice distortion and the electronic charge distribution are evident in multiple physical phenomena such as strong dependence of the

martensitic structure on the electronic concentration ratio e/a,[9] and softening of the acoustic [110]-TA$_2$ phonon mode caused by strong electron-phonon couplings.[20] Therefore, it can be conceived that the modulation of the local atomic environment will also lead to modulation of the electronic structure of the constituent elements and hence influence the magnetic structure of the alloy. The refined value for the overall magnetic moment for this alloy is 2.72 μ_B per Ni$_2$Mn$_{1.14}$Ga$_{0.86}$ formula unit, which is in excellent agreement with the saturation magnetic moment of 2.67 μ_B determined from bulk magnetic measurements. Below we take a critical look at the detailed magnetic configuration of the 5M structure, including moments on individual sites and site-specific modulation of magnetic moments.

In the present study, we found that the Mn atoms carry an average moment of $\sim$2.7 μ_B, consistent with the previous measurements of 2.4 μ_B for the austenite state and 2.9 μ_B for the martensite phase of Ni$_2$MnGa.[5,8] The refinement yielded small negative moments for Ni atoms and the Mn atoms on Ga sites. However, future characterization with polarized neutrons
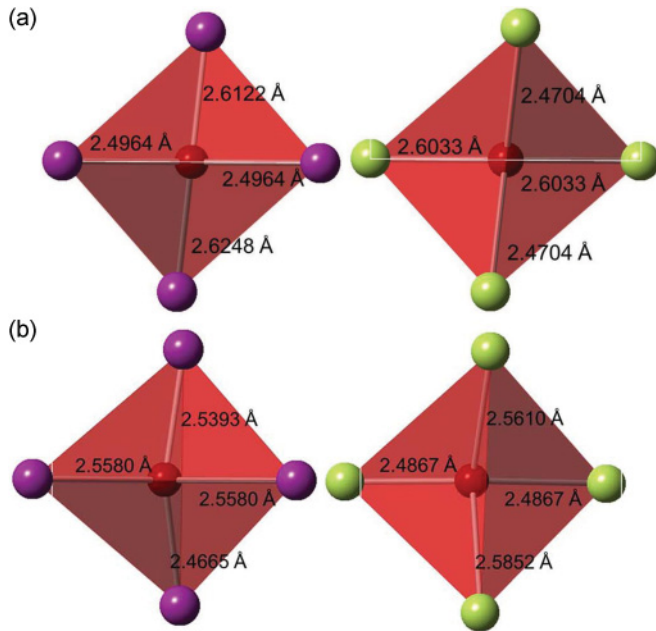
FIG. 8. (Color online) The shape of the Ni-Mn and the Ni-Ga tetrahedra for Ni at (a) $\bar{x}_4 = 0$ and (b) $\bar{x}_4 = 0.8$.

is necessary to accurately determine the small magnetic moments carried by Ni and Ga sites. Most significantly, consistent with earlier suggestions,[46] the magnetic moment on Mn was observed to be modulated in the current refinement.

Since the magnetic moments are carried by the Mn and Ni atoms, the magnetic structure of the alloy is expected to evolve from Ni-Ni, Ni-Mn, and Mn-Mn exchange interactions, which in turn depend on their bond lengths. The different bond distances for Ni-Mn and Mn-Mn are shown in Fig. 7. The modulation of the magnetic moments on the Mn sites, as shown in Figs. 7(c) and 7(d), are most likely to be influenced by the variations in the strength of exchange interactions due to changes in the local environments of Mn atoms, as evident from the Ni-Mn and Mn-Mn bond lengths. The magnetic moments on Mn were earlier shown to have a more localized character, based on first-principles calculations.[51] Particularly, due to magnetic coupling through conduction electrons between Mn atoms, which have a localized character, the magnetic properties of Ni-Mn-Ga alloys are extremely sensitive to Mn-Mn distances.[51] Consequently, shorter Mn-Mn bond distances tend to favor antiferromagnetic coupling between the atoms.[52,53] This correlates well with the observed magnetic moments on Mn1 at $\bar{x}_4 = 0$, 2. However, the modulation of magnetic moment on Mn2 seems to have a more complex electronic origin. During martensitic phase transition, a transfer of moments occurs from the Mn xy ($t2_g$) to the Ni $3z^2-r^2$ (e_g) orbitals.[8] Therefore, short Mn-Ni bond distances might be the critical factor for the low moments observed for both Mn1 at $\bar{x}_4 = 0$, 2 and for Mn2 at $\bar{x}_4 = 0.6$, 1.4.

Additionally, Mn on Ga sites prefers to antiferromagnetically couple with Mn on the Mn sites due to decrease in Mn-Mn bond distances.[51] In the present alloy, the additional Mn atoms are detected to substitute only on the Ga sites, while no Mn is present on the Ni sites. While this could not be definitely confirmed from x-ray powder diffraction,[26] neutron

diffraction unambiguously confirms this due to the difference in Mn and Ni neutron scattering lengths. Indeed, the best fit for the diffraction data is obtained when the average substitution ratio of Mn on Ga sites is modulated, as shown in Fig. 6. Therefore, for similar Mn-Mn and Mn-Ni bond distances, additional effects on the magnetic moments of Mn could be due to presence of Mn on Ga sites.

It is most likely that multiple structural and atomic substitution complexities, as detailed above for this nonstoichiometric alloy, influence the overall magnetic properties. It is also likely that, as a result of these coexisting effects, the magnetic moment on different sites are noncollinear and what is observed by neutron diffraction is an average projection of these noncollinear moments along the *b* axis. A detailed electronic structure calculation, taking into account atomic displacements, tetrahedral distortions, and atomic substitutions, is required to observe the combined effect of these multiple influences on the magnetic moments on various sites. It is expected that the results from the present neutron diffraction study would provide critical input and verifications to such calculations.

V. CONCLUSIONS

Analysis of single-crystal neutron diffraction data from a $Ni_2Mn_{1.14}Ga_{0.86}$ alloy yielded a monoclinic supercell crystal structure with a commensurate periodicity of $\vec{q} \sim 0.4\vec{c}$. As a result of better sensitivity of neutrons to the constituent elements (greater contrast in neutron scattering lengths) and their magnetic moments, the current analysis was successful in determining the different structural subtleties such as substitution of Mn on Ga sites, as well as 3D modulation of the atomic displacements and their magnetic moments. The current results, while supporting previous reports, provide new remarkable details including nonuniformity in the displacement modulations of the different atomic sites, site-specific tetrahedral distortions, and the correlations between the different structural modulations and site-specific magnetization. Further details regarding the weak magnetic moments on Ni and Ga sites are anticipated from future polarized neutron diffraction studies.

APPENDIX: DESCRIPTION OF (3 + 1)-D SPACE

A rigorous derivation of the relationship between the diffracted intensities and a description of the crystal structure in (3 + 1)-D space can be seen from texts such as Refs. 32 and 33 An introductory description of the concept is given below to facilitate better appreciation of the current article.
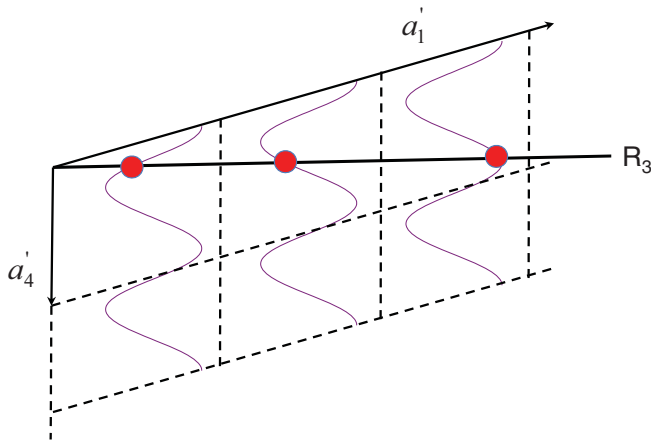
FIG. 9. (Color online) Representation of displacive structural modulation along $\vec{\mathbf{a}}_4'$. The waves indicate the amplitude of atomic displacement from their average lattice positions. The displacements along $\vec{\mathbf{a}}_4'$ are projected on the R_3 space at positions indicated by the red dots.

The structure of a normal crystal lattice can be entirely described by 3D translations of an unit cell with the base vectors $\vec{\mathbf{a}}_1$, $\vec{\mathbf{a}}_2$, and $\vec{\mathbf{a}}_3$; all the other elements of symmetry being completely defined within the unit cell. However, in a modulated crystal structure, in addition to 3D translations of a basic fundamental unit, the property p of an atom at a general position $(\bar{x}_1, \bar{x}_2, \bar{x}_3)$ is defined by a periodic function (not necessarily harmonic),

$$p\left(k_1\bar{x}_1 + k_2\bar{x}_2 + k_3\bar{x}_3\right), \tag{A1}$$

where the constants k_1, k_2, and k_3 define the modulation period, and in general at least one k_i could be an irrational number. The parameter p can be a fractional coordinate of the atomic position (viz. displacive modulation), an average occupational fraction (viz. substitutional modulation in nonstoichiometric alloys), or a magnetic moment (viz. magnetic modulation). In most simple cases, the modulation can be fully described by the introduction of an additional dimension $\bar{x}_4$. In this scheme, each atom in the 3D space R_3 is represented by a string in the 4D space R_4. The parameter p is now defined as

$$p\left(\bar{x}_4\right) = p\left(t + k_1\bar{x}_1 + k_2\bar{x}_2 + k_3\bar{x}_3\right), \tag{A2}$$

where t is the "phase" of the modulation and $\bar{x}_4$ is a function of t and $\bar{x}_i (i = 1, 2, 3)$. The modulated lattice in R_3 can be viewed as a section through the structure in R_4, and the properties of the atoms in the 3D crystal structure could be seen as manifestations of the string along certain sections with $t =$ constant.

The diffraction pattern from a modulated crystal is characterized by the presence of satellite peaks; the satellites appear at fractional coordinates in between the principal peaks. Each diffraction spot from a modulated crystal structure can therefore be fully indexed with

$$h_1\vec{\mathbf{b}}_1 + h_2\vec{\mathbf{b}}_2 + h_3\vec{\mathbf{b}}_3 + h_4\vec{\mathbf{b}}_4, \tag{A3}$$

where $\vec{\mathbf{b}}_i$ are the base vectors of the lattice B in the 3D reciprocal space and h_i are integers. Since they all appear in the 3D reciprocal space, one can write

$$\vec{\mathbf{b}}_4 = k_1\vec{\mathbf{b}}_1 + k_2\vec{\mathbf{b}}_2 + k_3\vec{\mathbf{b}}_3, \tag{A4}$$

where k_i could be an irrational number in general.

The base vectors $\vec{\mathbf{b}}_i'$ of the reciprocal lattice B' in R_4 is derived from the base vectors $\vec{\mathbf{b}}_i$ of the lattice B in R_3, following

$$\vec{\mathbf{b}}_1' = \vec{\mathbf{b}}_1, \quad \vec{\mathbf{b}}_2' = \vec{\mathbf{b}}_2,$$
$$\vec{\mathbf{b}}_3' = \vec{\mathbf{b}}_3, \quad \vec{\mathbf{b}}_4' = \vec{\mathbf{b}}_4 + \vec{\mathbf{e}}_4, \tag{A5}$$

where $\vec{\mathbf{e}}_4$ is perpendicular to the hyperplane R_3. In other words, B is obtained as a projection of B' along $\vec{\mathbf{e}}_4$. The corresponding set of vectors $\vec{\mathbf{a}}_i'$ reciprocal to $\vec{\mathbf{b}}_i'$ in R_4 are given by

$$\vec{\mathbf{a}}_1' = \vec{\mathbf{a}}_1 - k_1\vec{\mathbf{e}}_4, \quad \vec{\mathbf{a}}_2' = \vec{\mathbf{a}}_2 - k_2\vec{\mathbf{e}}_4,$$
$$\vec{\mathbf{a}}_3' = \vec{\mathbf{a}}_3 - k_3\vec{\mathbf{e}}_4, \quad \vec{\mathbf{a}}_4' = \vec{\mathbf{e}}_4, \tag{A6}$$

where the k_i now describe the modulation of the crystal, as described in the beginning of the section. The crystal lattice A (with base vectors $\vec{\mathbf{a}}_i$) in R_3 is obtained as a projection of the lattice A' (with base vectors $\vec{\mathbf{a}}_i$) in R_4, when the value of the parameter t,

$$t = -k_1\bar{x}_1 - k_2\bar{x}_2 - k_3\bar{x}_3 + \bar{x}_4, \quad \text{or}$$
$$t = -\vec{\mathbf{q}} \cdot \vec{\mathbf{r}} + \bar{x}_4, \tag{A7}$$

is equal to zero. In the above expression, $\vec{\mathbf{q}}$ is the modulation vector, and $\vec{\mathbf{r}}$ is the position vector for the atom in the basic average structure.

In essence, the (3 + 1)-D superspace can be viewed as a mathematical tool which can be used to conveniently describe certain modulations which are not necessarily commensurate with the basic unit cell. Even for modulations which are commensurate, a superspace approach could be a powerful tool to simultaneously describe multiple modulations, for which convergence to a structure solution would be rather difficult following a conventional 3D approach.

An illustrative example of the (3 + 1)-D superspace is shown in Fig. 9, where the atoms are displaced from their average positions following displacive modulations of a crystal structure. The displacement modulation along $\vec{\mathbf{a}}_4'$ is manifested in the crystal lattice in R_3, whenever the condition (A7) is satisfied.

*wangxl@ornl.gov

[1] M. Chmielus, X. X. Zhang, C. Witherspoon, D. C. Dunand, and P. Mullner, Nat. Mater. **8**, 863 (2009).

[2] P. Müllner, V. A. Chernenko, and G. Kostorz, Scr. Mater. **49**, 129 (2003).

[3] L. Straka and O. Heczko, J. Magn. Magn. Mater. **290-291**, 829 (2005).

[4] K. Ullakko, J. K. Huang, C. Kantner, R. C. O. Handley, and V. V. Kokorin, Appl. Phys. Lett. **69**, 1966 (1996).

[5] P. J. Brown, J. Crangle, T. Kanomata, M. Matsumoto, K.-U. Neumann, B. Ouladdiaf, and K. R. A. Zieback, J. Phys. Condens. Matter **14**, 10159 (2002).

[6] V. A. Chernenko, C. Seguí, E. Cesari, J. Pons, and V. V. Kokorin, Phys. Rev. B **57**, 2659 (1998).

[7] M. Richard, J. Feuchtwanger, D. Schlagel, T. Lograsso, S. M. Allen, and R. C. O'Handley, Scr. Mater. **54**, 1797 (2006).

[8] P. J. Brown, A. Y. Bargawi, J. Crangle, K.-U. Neumann, and K. R. A. Zieback, J. Phys.: Condens. Matter **11**, 4715 (1999).

[9] V. A. Chernenko, Scr. Mater. **40**, 523 (1999).

[10] P. J. Webster, K. R. A. Ziebeck, S. L. Town, and M. S. Peak, Philos. Mag. B **49**, 295 (1984).

[11] Z. Nishiyama, *Martensitic Transformation* (Academic Press, New York, 1978).

[12] V. V. Kokorin and V. Chernenko, Phys. Met. Metallogr. **68**, 111 (1989).

[13] V. V. Martynov and V. V. Kokorin, J. Phys. III Fr. **2**, 739 (1992).

[14] S. Morito and K. Otsuka, Mater. Sci. Eng., A **208**, 47 (1996).

[15] S. Muto and D. Schryvers, J. Alloys Compd. **199**, 1 (1993).

[16] Y. Noda, S. M. Shapiro, G. Shirane, Y. Yamada, and L. E. Tanner, Phys. Rev. B **42**, 10397 (1990).

[17] D. Schryvers and L. E. Tanner, Ultramicroscopy **32**, 241 (1990).

[18] A. G. Khachaturyan, S. M. Shapiro, and S. Semenovskaya, Phys. Rev. B **43**, 10832 (1991).

[19] S. Kaufmann, U. K. Rossler, O. Heczko, M. Wuttig, J. Buschbeck, L. Schultz, and S. Fahler, Phys. Rev. Lett. **104**, 145702 (2010).

[20] A. Zheludev, S. M. Shapiro, P. Wochner, and L. E. Tanner, Phys. Rev. B **54**, 15045 (1996).

[21] I. Glavatskyy, N. Glavatska, I. Urubkov, J. U. Hoffman, and F. Bourdarot, Mater. Sci. Eng., A **481-482**, 298 (2008).

[22] J. Pons, V. A. Chernenko, R. Santamarta, and E. Cesari, Acta Mater. **48**, 3027 (2000).

[23] J. Pons, R. Santamarta, V. A. Chernenko, and E. Cesari, J. Appl. Phys. **97**, 083516 (2005).

[24] L. Righi, F. Albertini, G. Calestani, L. Pareti, A. Paoluzi, C. Ritter, P. A. Algarabel, L. Morellon, and M. Ricardo Ibarra, J. Solid State Chem. **179**, 3525 (2006).

[25] L. Righi, F. Albertini, A. Paoluzi, S. Fabbrici, E. Villa, G. Calestani, and S. Besseghini, Mater. Sci. Forum **635**, 33 (2010).

[26] L. Righi, F. Albertini, L. Pareti, A. Paoluzi, and G. Calestani, Acta Mater. **55**, 5237 (2007).

[27] L. Righi, F. Albertini, E. Villa, A. Paoluzi, G. Calestani, V. Chernenko, S. Besseghini, C. Ritter, and F. Passaretti, Acta Mater. **56**, 4529 (2008).

[28] P. Molnar, P. Sittner, P. Lukas, S.-P. Hannula, and O. Heczko, Smart Mater. Struct. **17**, 035014 (2008).

[29] S. J. Murray, M. Marioni, S. M. Allen, R. C. O. Handley, and T. A. Lograsso, Appl. Phys. Lett. **77**, 886 (2000).

[30] M. Dusek, V. Petricek, M. Wunschel, R. E. Dinnebier, and S. van Smaalen, J. Appl. Crystallogr. **34**, 398 (2001).

[31] O. Gourdon, Z. Izaola, L. Elcoro, V. Petricek, and G. J. Miller, Inorg. Chem. **48**, 9715 (2009).

[32] T. Janssen, A. Janner, A. Looijenga-Vos, and P. M. de Wolff, in *International Tables for Crystallography*, edited by E. Prince (Kluwer Academic, Dordrecht, 2006), Vol. C, p. 907.

[33] P. M. De Wolff, Acta Crystallogr. A **30**, 777 (1974).

[34] X. L. Wang, T. M. Holden, G. Q. Rennich, A. D. Stoica, P. K. Liaw, H. Choo, and C. R. Hubbard, Physica B **385-386**, 673 (2006).

[35] T. E. Mason, D. Abernathy, I. Anderson, J. Ankner, T. Egami, G. Ehlers, A. Ekkebus, G. Granroth, M. Hagen, K. Herwig, J. Hodges, C. Hoffmann, C. Horak, L. Horton, F. Klose, J. Larese, A. Mesecar, D. Myles, J. Neuefeind, M. Ohl, C. Tulk, X.-L. Wang, and J. Zhao, Physica B **385-386**, 955 (2006).

[36] [http://neutrons.ornl.gov/instruments/SNS/factsheets/Instrument_7.pdf].

[37] [http://neutrons.ornl.gov/instruments/SNS/factsheets/Instrument_12.pdf].

[38] X. L. Wang, C. Stassis, D. C. Johnston, T. C. Leung, J. Ye, B. N. Harmon, G. H. Lander, A. J. Schultz, C.-K. Loong, and J. M. Honig, Phys. Rev. B **45**, 5645 (1992).

[39] D. Mikkelson, R. Mikkelson, A. J. Schultz, C. Hoffmann, and X. P. Wang, http://ftp.sns.gov/ISAW/; A. Chatterjee, D. Mikkelson, R. Mikkelson, J. Hammonds, and T. Worlton, Appl. Phys. A **74**, s194 (2002).

[40] J. Zikovsky, P. F. Peterson, X. P. Wang, M. Frost, and C. Hoffmann, J. Appl. Crystallogr. **44**, 418 (2011).

[41] V. Petricek, M. Dusek, and L. Palatinus, JANA2006 (Institute of Physics, Praha, Czech Republic, 2006).

[42] R. Ranjan, S. Banik, S. R. Barman, U. Kumar, P. Mukhopadhyay, and D. Pandey, Phys. Rev. B **74**, 224443 (2006).

[43] F.-X. Hu, B.-G. Shen, and J.-R. Sun, Appl. Phys. Lett. **76**, 3460 (2000).

[44] X. Zhou, W. Li, H. P. Kunkel, and G. Williams, J. Phys. Condens. Matter **16**, L39 (2004)

[45] A. Rauch and W. Waschkowski, in *Neutron Data Booklet*, edited by A.-J. Dianoux and G. Lander (Institut Laue-Langevin by license under the OCPScience imprint, 2003), p. 1.1.

[46] P. J. Brown, A. P. Gandy, T. Kanomata, M. Matsumoto, K. Neumann, K.-U. Neumann, A. Sheikh, and K. R. A. Ziebeck, Mater. Sci. Forum **583**, 285 (2008).

[47] P. J. Brown, A. P. Gandy, K. Ishida, R. Kainuma, T. Kanomata, M. Matsumoto, H. Morito, K.-U. Neumann, K. Oikawa, B. Ouladdiaf, and K. R. A. Ziebeck, J. Magn. Magn. Mater. **310**, 2755 (2007).

[48] A. T. Zayak and P. Entel, Mater. Sci. Eng., A **378**, 419 (2004).

[49] P. A. Bhobe, K. R. Priolkar, and P. R. Sarode, Phys. Rev. B **74**, 224425 (2006).

[50] A. T. Zayak, P. Entel, J. Enkovaara, A. Ayuela, and R. M. Nieminen, J. Phys. Condens. Matter **15**, 159 (2003).

[51] J. Enkovaara, A. Ayuela, J. Jalkanen, L. Nordström, and R. M. Nieminen, Phys. Rev. B **67**, 054417 (2003).

[52] V. D. Buchelnikov, V. V. Sokolovskiy, H. C. Herper, H. Ebert, M. E. Gruner, S. V. Taskaev, V. V. Khovaylo, A. Hucht, A. Danneberg, M. Ogura, H. Akai, M. Acet, and P. Entel, Phys. Rev. B **81**, 094411 (2010).

[53] J. Enkovaara, O. Heczko, A. Ayuela, and R. M. Nieminen, Phys. Rev. B **67**, 212405 (2003).